

Overcoming photon blockade in circuit QED single-atom maser with engineered metastability and strong coupling

A.A. Sokolova,^{1,2,3,4} D.A. Kalacheva,^{5,2,3,1} G.P. Fedorov,^{1,2,3,*} and O.V. Astafiev^{5,2}

¹*Russian Quantum Center, Skolkovo village, Russia*

²*Moscow Institute of Physics and Technology, Dolgoprudny, Russia*

³*National University of Science and Technology MISIS, Moscow, Russia*

⁴*Institute of Science and Technology Austria, 3400 Klosterneuburg, Austria*

⁵*Skolkovo Institute of Science and Technology, Moscow, Russia*

(Dated: September 13, 2022)

Reaching high cavity population with a coherent pump in the strong-coupling regime of a single-atom laser is impossible due to the photon blockade effect. In this work, we experimentally demonstrate that in a single-atom maser based on a transmon strongly coupled to two resonators it is possible to pump over a dozen of photons into the system. The first high-quality resonator plays a role of usual lasing cavity, and the second one presents a controlled dissipation channel, bolstering population inversion, and modifies the energy level structure to lift the blockade. As a confirmation of lasing action, we observe conventional laser features such as the narrowing of emission linewidth and external signal amplification. Additionally, we report unique single-atom features: self-quenching and several lasing thresholds.

I. INTRODUCTION

Experimental studies on single-atom lasers and masers are following the recent developments in quantum optics of individual quantum systems [1]. Trapped atoms/ions [2, 3], superconducting artificial atoms [4–6], semiconductor double quantum dots [7–9], biased Josephson junctions [10] have already been used as a single-atom gain medium and allowed experimental investigation of non-conventional properties of these lasers such as multistability, emission of squeezed radiation, self-quenching, etc. Recently, there was a theoretical proposal [11] regarding a superconducting circuit QED [12] maser consisting of a magnetic-flux-tunable Xmon-type transmon [13] coupled to two microwave resonators: a high-Q reservoir to accumulate microwave photons, and a low-Q auxiliary one. The latter cavity forms an engineered dissipative environment enforcing metastability of the second excited transmon state. Besides bolstering the population inversion, it also significantly modifies the maser energy level structure and allows it to overcome the photon blockade limiting the intensity of the emitted radiation in coherently-pumped systems with strong coupling [14, 15]. Physical realization of the proposed device would allow one to study those its properties that cannot be explored in numerical simulations, for example the spectrum of the emitted radiation which is hard to compute [16]. Additionally, we expect that suggested architecture will be suitable for novel quantum devices, for example, coherent quantum phonon emitters, which have a wide range of both scientific and practical applications [17]. In this paper, we describe our implementation of the suggested architecture and present main results confirming the lasing action of the device.

II. DEVICE

In Fig. 1(a), we reproduce the conceptual schematic of the device from the proposal [11]. The Hamiltonian of the system in the laboratory frame

$$\hat{H} = \hat{H}_t + \sum_{\lambda=r,a} (\hat{H}_c^{(\lambda)} + \hat{H}_i^{(\lambda)}), \quad (1)$$

$$\hat{H}_t = hf_{ge}^{\max} b^\dagger b + \frac{h\alpha}{2} b^\dagger b (b^\dagger b - 1), \quad (2)$$

$$\hat{H}_c^{(\lambda)} = hf_{(\lambda)} (a_\lambda^\dagger a_\lambda + 1/2), \quad (3)$$

$$\hat{H}_i^{(\lambda)} = \hbar g_\lambda (ba_\lambda^\dagger + b^\dagger a_\lambda), \quad (4)$$

where \hat{H}_t , $\hat{H}_c^{(\lambda)}$ and $\hat{H}_i^{(\lambda)}$ are the transmon, cavity and interaction Hamiltonians, where $a_{r,a}$, b are the bosonic annihilation operators for the reservoir, auxiliary resonator and transmon. The cavities are designed to have coupling strengths $g_{r,a}$ and leakage rates $\kappa_{r,a}$. The design values for these parameters have been optimized for maximal steadystate reservoir population N_{ss} [11]. The relevant GKSL master equation is based on the collapse operators $\sqrt{\kappa_{r,a}} a_{r,a}$, $\sqrt{\gamma} b$ for the relaxation of the cavities and the transmon and $\sqrt{\gamma_\phi} b^\dagger b$ for transmon pure dephasing. For comparison between the design parameters and the parameters found experimentally in this work, along with the brief description of their meaning, see Table I. The transmon frequency is maximal for zero external flux through its SQUID loop (around 5.95 GHz) and can be tuned down in frequency into resonance consecutively with the reservoir and auxiliary cavity:

$$f_{ge}(\Phi_e) \approx f_{ge}^{\max} \sqrt{\cos(\pi\Phi_e/\Phi_0)}, \quad (5)$$

where Φ_e/Φ_0 is the ratio of the external flux through the SQUID to the magnetic flux quantum. There is a slight discrepancy between the anharmonicity of the transmon and the frequency difference between the cavities (180 MHz vs. 145 MHz), and appreciable deviations in κ_a and g_a from design

* gleb.fedorov@phystech.edu

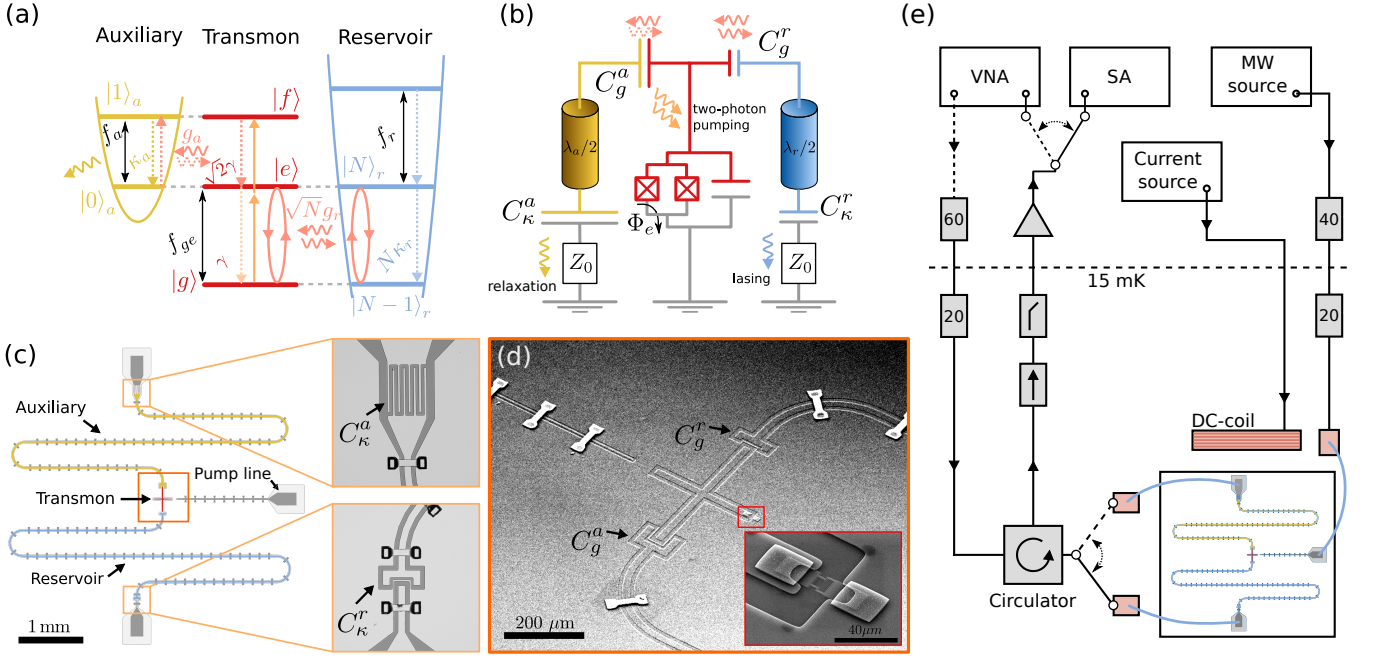


FIG. 1. (a) A scheme showing the configuration of the energy levels when the reservoir is resonant with the $|g\rangle \leftrightarrow |e\rangle$ transition, and the auxiliary cavity is resonant with the $|e\rangle \leftrightarrow |f\rangle$ transition. (b) Schematic of the circuit QED implementation of the system. To the left is the auxiliary and to the right is the reservoir cavity, implemented as halfwave transmission line (coplanar waveguide) resonators. Capacitors $C_{\kappa}^{r,a}$ couple transmon with the reservoir, auxiliary cavity; $C_{\kappa}^{r,a}$ define desired external quality factors. (c) Design of the device (photo-lithography layer) and optical images of the cavity coupling capacitors. Microwave antenna routing the pump signal towards the transmon comes from the right side of the sample. The colors of the elements correspond to the colors on (a) and (b). (d) SEM image of the transmon coupled to the cavities; in the inset, the SQUID area is shown with higher magnification. (e) Scheme of measurement: sample as in (c) is wirebonded, refrigerated to 15 mK, input signals come through attenuated coaxial lines, and output line contains an amplifier chain with a HEMT amplifier. By one switch one chooses whether to measure reflection off auxiliary or reservoir resonator, and by another signal analyzer (SA) and vector network analyzer (VNA) are exchanged; an external solenoid supplies DC magnetic field to the SQUID.

values. This mismatch does not critically affect the functioning of the device by virtue of general robustness of the optimal N_{ss} to parameter perturbations for large values of κ_a . Another difference is the non-negligible internal loss of the reservoir cavity which we estimate from the fit to be $\kappa_r^i = \kappa_r - \kappa_r^e = 0.39 \mu\text{s}^{-1}$ in the worst case (see Supplementary Materials). As N_{ss} in the simple model is inversely proportional to total reservoir loss [11], and as the internal loss in our case approximately equals the external, one can expect halving of the device maximum emission intensity compared to the ideal case. We take κ_r^e into account when calculating the N_{ss} from measured signal power. Finally, we note that the proper relaxation and coherence times of the transmon were not measured directly due to the limitations of the experimental setup; one can expect its relaxation rate to be lower than κ_r^i due to a lower interface participation ratio [18], while the dephasing can be neglected as the system functions in the mixed state [11].

The electrical scheme of the device and the design for nanofabrication are shown in Fig. 1(b,c). The couplings and dissipation rates are physically determined by the capacitances $C_{\kappa}^{a,r}$ which are small enough to be produced in a single Al layer. However, as they break the ground plane, we also use air-bridges to ensure the uniformity of ground electric potential. In Fig. 1(d) we show a SEM image of the Xmon along

Parameter	Meaning	Measured	Design
f_r	reservoir cavity frequency	5.860 GHz	6 GHz
κ_r	res. total decay rate	$0.69 \mu\text{s}^{-1}$	$0.31 \mu\text{s}^{-1}$
κ_r^e	res. decay rate to feedline	$0.3 \mu\text{s}^{-1}$	$0.31 \mu\text{s}^{-1}$
$g_r/2\pi$	res.-transmon coupling	11 MHz	6.5 MHz
f_a	auxiliary cavity frequency	5.715 GHz	5.8 GHz
κ_a	aux. total decay rate	$90 \mu\text{s}^{-1}$	$138 \mu\text{s}^{-1}$
$g_a/2\pi$	aux.-transmon coupling	15.5 MHz	23.5 MHz
f_{ge}^{max}	zero-flux transmon frequency	5.95 GHz	6.5 GHz
α	transmon anharmonicity	180 MHz	200 MHz
$f_r - f_a$	res.-aux. cavity detuning	145 MHz	200 MHz

TABLE I. Summary of the device parameters, measured vs. planned in the design. Associated with dielectric loss, the reservoir total decay rate κ_r depends strongly on the measurement power, and the highest value is given here.

with its SQUID in the inset (see Supplementary Materials for fabrication details).

III. REFLECTION AND EMISSION SPECTROSCOPY

We begin the study of the system by performing reflection spectroscopy of the reservoir resonator when the transmon is tuned into resonance with it, see Fig. 2(a). The vector network analyzer (VNA) measuring the complex reflection parameter S_{11} is set at a low power near the single-photon regime for the reservoir cavity (frequency sweep range of the VNA is shown on the y -axis). While performing spectroscopy, we send an additional signal at $f_p = f_{gf}/2 = 5.788$ GHz to the pump line using a separate microwave source. Its power is shown on the x -axis. When its power is off or very low, two transitions of the avoided crossing $|0_a, g, 0_r\rangle \rightarrow (|0_a, g, 1_r\rangle \pm |0_a, e, 0_r\rangle)/\sqrt{2}$ are visible at 5.854 and 5.876 GHz, from what $g_r/2\pi = 11$ MHz (see Supplementary Materials). When the two-photon pumping power is increased, these transitions become Stark-shifted upwards and saturate. They completely disappear at around -10 dBm level of the microwave source, which is the beginning of the lasing action. The $|S_{11}|$ characteristic of the remaining spectral line is not a Lorentzian dip above this power but shows small amplification – manifestation of the injection locking effect [19]. Also, above -10 dBm the reservoir begins to emit power (Fig. 2(b)) which can be detected upon disconnecting the VNA from the measurement setup and connecting a signal analyzer (SA) to the output line.

Precise calibration of the emission power is difficult due to the uncertainty of the amplification level in the output line. We find it by using the fact that the vacuum Rabi splitting can be regarded as an effective two-level system, for which calibration of absolute input power is feasible [20, 21]. First, we measure the saturation of the avoided crossing peaks with increase of VNA power P_{VNA} and compare the data with numerical simulation for the extracted system parameters; this allows us to find the driving amplitude, and thus the absolute signal power $P_{\text{c.p.}}$ at the reservoir coupling port for a given P_{VNA} . Next, we measure the power of a slightly off-resonant reflected and amplified signal P_{SA} by the SA assuming almost unity reflection off the coupling port in the vicinity of the resonance. Finally, calculate the amplification level $a = P_{\text{SA}}/P_{\text{c.p.}}$ in the output line (see details in the Supplementary Materials). When the amplification is known, the total emission power at the coupling port can be calculated as an integral of the signal power spectral density $S_{VV}(f)$ measured by the signal analyzer as

$$P = \kappa_r^e N_{\text{ss}} \hbar \omega = \frac{1}{a} \int_{\text{BW}} S_{VV}(f) df, \quad (6)$$

where BW stands for the bandwidth where the emission signal is non-negligible. For this value, we take the span of the SA shown in the y -axis of Fig. 2(b). We plot the calibrated N_{ss} vs. pumping power in Fig. 2(c) and confirm that it is indeed possible to achieve significant reservoir population using our architecture: in the range between 5 and 10 dBm of pumping power, reservoir accumulates nearly 20 photons. According to the model described in the proposal and generalized to the case of non-zero detuning between the transitions $g \rightarrow e$ and $|0\rangle_a \rightarrow |1\rangle_a$, for experimental parameters the system should

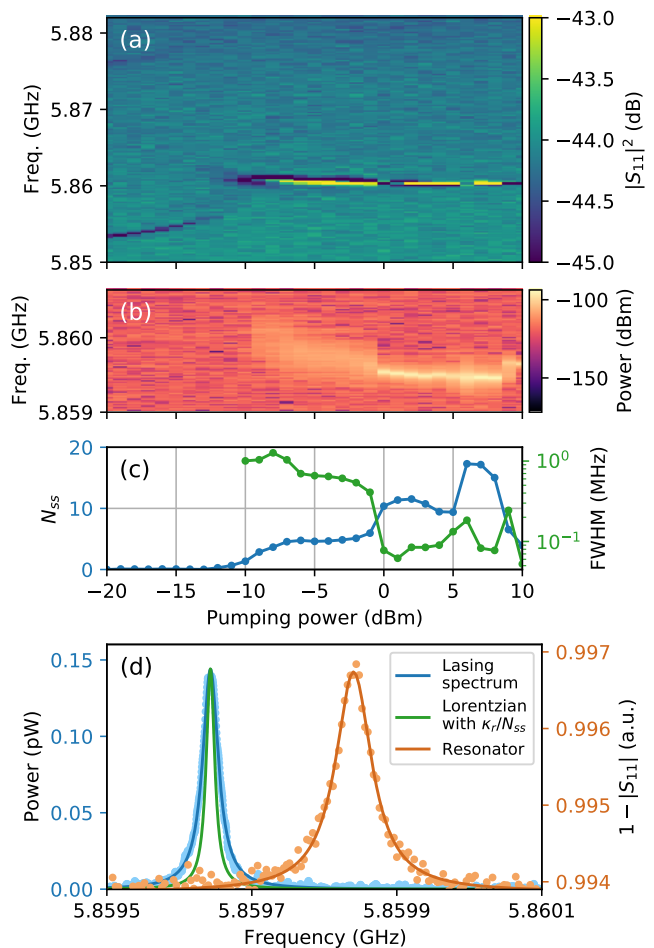


FIG. 2. (a) Reflection spectroscopy of the transmon-resonator avoided crossing vs. the two-photon pumping power, pumping frequency $f_p = 5.788$ GHz, VNA signal power is at -50 dBm. (b) Measured emission spectrum from the reservoir cavity vs. the pumping power. (c) Estimated number of photons in the reservoir N_{ss} and the spectral linewidth calculated from (b) by Lorentzian fitting. (d) Lasing spectrum (blue, FWHM: 26 kHz) for 10 dBm pumping power compared with the resonator reflection profile for the same photon population ($N_{\text{ss}} = 3.9$, orange, 61 kHz) and the Schawlow-Townes limit (green, 16 kHz).

accumulate around 24 photons, which is in a good agreement with data. Using a numerical model with the experimental parameters, we find even better agreement for maximal N_{ss} around 19 (for details on both approaches, see Supplementary Materials).

In Fig. 2(c), one can observe four lasing thresholds in N_{ss} located at -10, -1, 5 and 8 dBm which are accompanied by changes in the emission linewidth and lasing frequency. This behavior is probably connected with the special energy level structure of the system [11] and can be qualitatively reproduced in simulations (see Supplementary Materials). After the last threshold, there is a significant decrease of N_{ss} , which we identify as the self-quenching effect [22].

Finally, in Fig. 2(d) we compare the lasing spectrum and

reservoir cavity response, which both can be well approximated by Lorentzian curves. The orange line shows $1 - |S_{11}|$ when the transmon is far detuned, and the blue line is the lasing spectrum at 10 dBm pumping power. The central frequency of the latter is 200 kHz lower than f_r , which may be explained by the fact that frequencies of the transitions between high energy levels are not equal to f_r due to strong coupling [11]. For high reservoir population, the line of the emission spectrum is significantly narrower than the resonator proper amplitude characteristic: the FWHM is 26 kHz vs. 61 kHz for $N_{ss} = 3.9$, and approaches the Schawlow-Townes-limited spectrum with a width of $\kappa_r/2\pi N_{ss} = 16$ kHz.

As an additional test for the laser action of the device, we show that an external microwave signal is amplified upon reflection off the reservoir cavity when the system is pumped above the first threshold. The results are presented in Fig. 3 for three different pumping powers: -5 dBm (a), 5 dBm (b) and 10 dBm (c). The reference level is depicted by a horizontal black line, and the dip in the data trace means resonant absorption of radiation, while the peak reveals amplification. Amplification depends non-linearly on the pumping power, with a maximum amplitude gain of $G = 3.6$ at 5 dBm pumping power. In Fig. 3(d), one can see how the amplification saturates with increased VNA power for the three values of pumping power, which is a typical behavior [19]. We also observe that in Fig. 3(a) the amplification area is located slightly below resonance, while in Fig. 3(b-c) it is slightly above. Based on the data shown in Fig. 2(a), we find that the transition between these regimes occurs at 0 dBm of pumping power, and it coincides with the second lasing threshold in Fig. 2(c); the nature of this effect remains unclear to us.

In order to quantify the device action outside the optimal regime and better understand the lasing mechanism, we also study the dependence of the emission spectrum on the external flux in the SQUID and the pumping frequency. We now use lower-power pumping (-5 dBm) to avoid power broadening and achieve better resolution of transitions. Fig. 4(a) shows scan of two symmetric avoided crossings with green lines marking the points where the transmon ge transition is resonant with the reservoir, and yellow lines – where the ge transition is resonant with the pump signal. The first configuration was studied before in Fig. 1(a), and in the second one the qubit may be pumped directly. As can be seen in Fig. 4(b) and (c), the reservoir population is the highest in proximity to the green lines, both in the experiment and the simulation. Nevertheless, we note that emission is observed for a wider frequency range in the experiment than in the simulation. A small dip in N_{ss} which coincides with the central points of the avoided crossings can be explained by the fact that low-power pumping cannot overcome the photon blockade, being under the lasing threshold [11].

Similarly, we measure the dependence of the emission spectrum on the pumping frequency for the resonant configuration. The results are shown in Fig. 4(d). Since there is a 35 MHz detuning between $f_r + f_a$ and f_{gf} when $f_{ge} = f_r$, we mark two competing cases of two-photon pumping: the magenta vertical line corresponds to the resonance with the transition from the ground state to $|1_a, e, 0_r\rangle$ (this is the con-

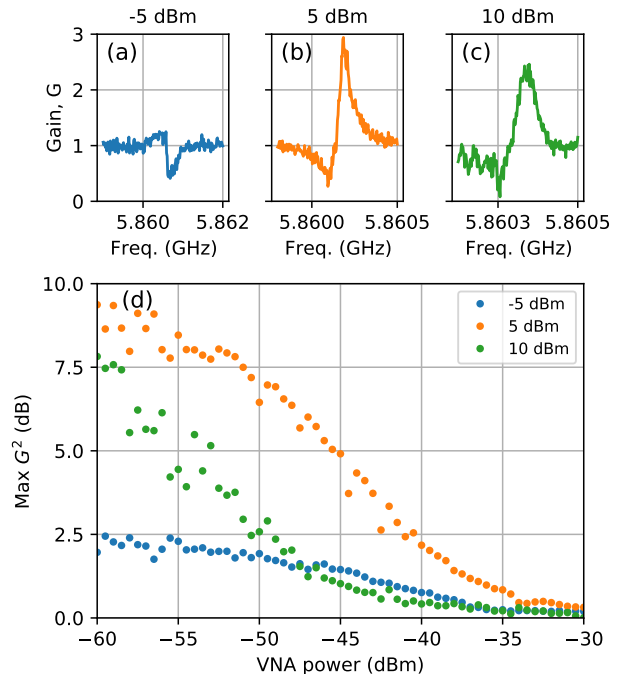


FIG. 3. (a-c) Gain of reflection amplitude vs. frequency for pumping powers -5, 5 and 10 dBm, respectively, at the VNA power of -60 dBm. (d) Maximum value of the power gain over the frequency range shown on the x -axes in (a-c) depending on the VNA power for three pumping powers.

figuration chosen in Fig. 2), and the cyan one – to $|0_a, f, 0_r\rangle$. In Fig. 4(e), two areas of high emission attributed to these processes are clearly visible. We find that in contrast with the simulation, in the experiment both pumping frequencies give comparable values for the integrated emission power and the corresponding photon number in the reservoir; however, pumping at $f_{gf}/2$ gives a wider emission line than at $(f_r + f_a)/2$. We also note the asymmetry of the emission areas with respect to the corresponding marker lines, showing a notable shift towards higher pump frequencies.

IV. DISCUSSION

In this work, we have implemented a single-atom maser based on a transmon that overcomes the photon blockade in the strong coupling regime, concluding previous theoretical study on the subject. We were able to pump more than 15 photons in cavity, a notably high population for a coherent pump in this class of systems [3, 11, 14, 15]. Additionally, we observed several lasing thresholds and self-quenching accompanied by variations in emission spectrum central frequency and linewidth despite that usually single-atom lasers in the strong-coupling regime are thresholdless [2, 3, 23]. We explain the possibility of overcoming the photon blockade in our device by the additional splittings in the level structure

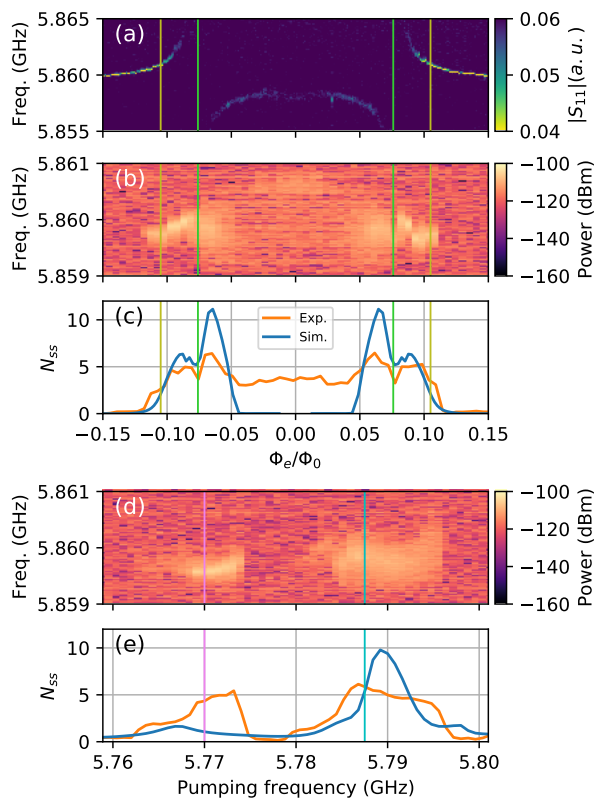


FIG. 4. **(a)** Reflection spectroscopy of the avoided crossing at -60 dBm on the VNA vs. magnetic flux Φ_e through the transmon SQUID. Green lines mark the points of transmon-reservoir resonance and yellow lines show Φ_e where the ge frequency is equal to the pumping frequency. **(b)** Lasing spectrum vs. Φ_e for pumping power of -5 dBm at 5.788 GHz. **(c)** Reservoir N_{ss} , experiment (orange) and simulation (blue) vs. Φ_e . **(d)** Lasing spectrum depending on the pump frequency when its power is -5 dBm. Magenta line is the two-photon frequency of $|g\rangle \leftrightarrow |1\rangle_a$ process, cyan line – of $|g\rangle \leftrightarrow |f\rangle$ process. **(e)** Number of photons in the reservoir resonator vs. pumping power, experiment (orange) and simulation (blue).

emerging from coupling to auxiliary resonator and ensuring resonance condition for the two-photon pump for high populations. Besides, based on theoretical studies we assume that our system should exhibit such features as bistability of Wigner function and sub-Poissonian statistics of emitted radiation [11].

As this was the first experimental study of this kind of a device, we have also investigated in more detail the conventional manifestations of the lasing effect to confirm its nature. Firstly, we have demonstrated that the emission linewidth is narrower than the resonator proper linewidth and, notably, approaches the Schawlow-Townes limit for certain regimes. Secondly, if supplied, an external microwave signal is being amplified by the device; this effect was previously demonstrated for single-atom masers [4] as well as in ordinary lasers and is caused by injection-locking effect [19]. Finally, we measured the emission spectrum depending on transmon frequency and pumping frequency and observed that lasing manifests itself when the system parameters are close to the theoretically predicted, which is a strong evidence of the correctness of our model.

V. ACKNOWLEDGMENTS

We thank N.N. Abramov for assistance with the experimental setup. The sample was fabricated using equipment of MIPT Shared Facilities Center. This research was supported by Russian Science Foundation, grant no. 21-72-30026.

-
- [1] S. Haroche and J.-M. Raimond, *Exploring the quantum: atoms, cavities, and photons* (Oxford university press, 2006).
- [2] J. McKeever, A. Boca, A. D. Boozer, J. R. Buck, and H. J. Kimble, *Nature* **425**, 268 (2003).
- [3] F. Dubin, C. Russo, H. G. Barros, A. Stute, C. Becher, P. O. Schmidt, and R. Blatt, *Nature Physics* **6**, 350 (2010).
- [4] O. Astafiev, K. Inomata, A. Niskanen, T. Yamamoto, Y. A. Pashkin, Y. Nakamura, and J. S. Tsai, *Nature* **449**, 588 (2007).
- [5] P. Neillinger, M. Reháč, M. Grajcar, G. Oelsner, U. Hübner, and E. Il'ichev, *Physical Review B* **91**, 104516 (2015).
- [6] P. Neillinger, S. N. Shevchenko, J. Bogár, M. Reháč, G. Oelsner, D. S. Karpov, U. Hübner, O. Astafiev, M. Grajcar, and E. Il'ichev, *Physical Review B* **94**, 094519 (2016).
- [7] M. Nomura, N. Kumagai, S. Iwamoto, Y. Ota, and Y. Arakawa, *Nature Physics* **6**, 279–283 (2010).
- [8] Y. Y. Liu, K. D. Petersson, J. Stehlik, J. M. Taylor, and J. R. Petta, *Physical Review Letters* **113**, 1 (2014), 1401.7730.
- [9] Y.-Y. Liu, J. Stehlik, C. Eichler, X. Mi, T. R. Hartke, M. J. Gullans, J. M. Taylor, and J. R. Petta, *Physical Review Letters* **119**, 097702 (2017).
- [10] M. Cassidy, A. Bruno, S. Rubbert, M. Irfan, J. Kammhuber, R. Schouten, A. Akhmerov, and L. Kouwenhoven, *Science* **355**, 939 (2017).
- [11] A. Sokolova, G. Fedorov, E. Il'ichev, and O. Astafiev, *Physical Review A* **103**, 013718 (2021).
- [12] A. Blais, A. L. Grimsmo, S. M. Girvin, and A. Wallraff, *Reviews of Modern Physics* **93**, 025005 (2021).
- [13] R. Barends, J. Kelly, A. Megrant, D. Sank, E. Jeffrey, Y. Chen, Y. Yin, B. Chiaro, J. Mutus, C. Neill, *et al.*, *Physical review letters* **111**, 080502 (2013).
- [14] K. M. Birnbaum, A. Boca, R. Miller, A. D. Boozer, T. E. Northup, and H. J. Kimble, *Nature* **436**, 87 (2005).
- [15] A. Imamoglu, H. Schmidt, G. Woods, and M. Deutsch, *Physical review letters* **79**, 1467 (1997).

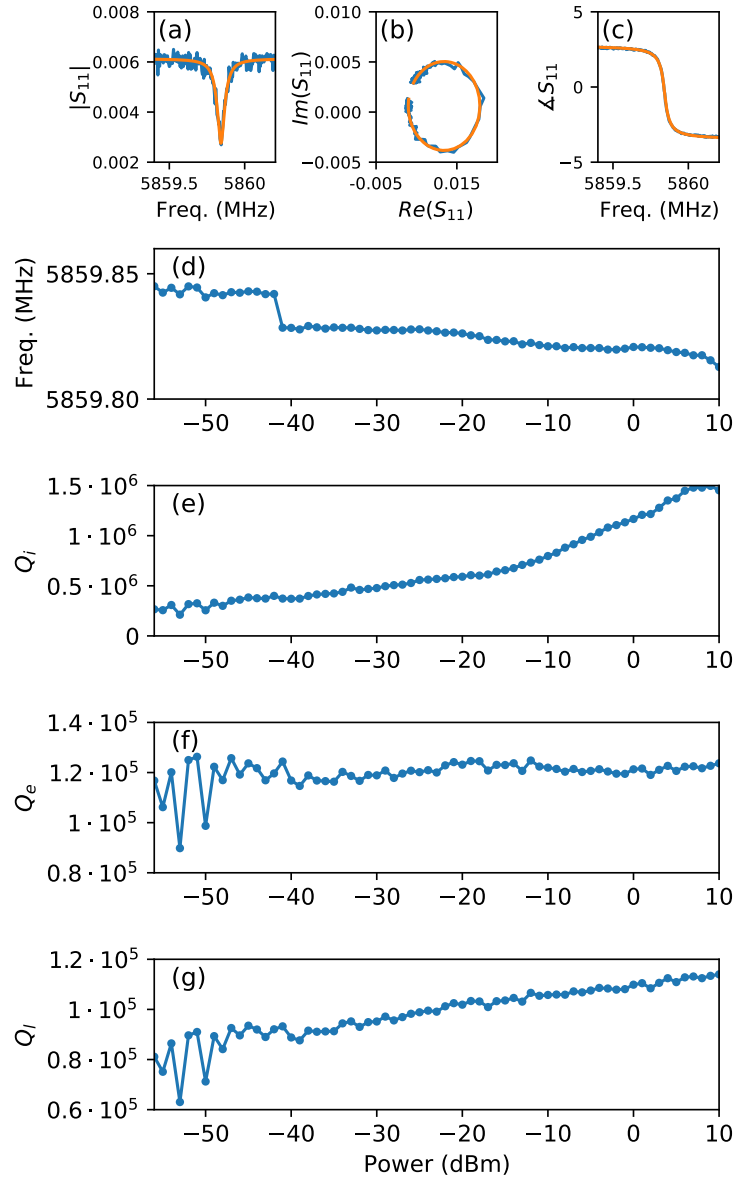
- [16] M. Löffler, G. M. Meyer, and H. Walther, *Physical Review A* **55**, 3923 (1997).
- [17] A. N. Bolgar, J. I. Zotova, D. D. Kirichenko, I. S. Besedin, A. V. Semenov, R. S. Shaikhaidarov, and O. V. Astafiev, *Physical Review Letters* **120**, 223603 (2018).
- [18] C. Wang, C. Axline, Y. Y. Gao, T. Brecht, Y. Chu, L. Frunzio, M. Devoret, and R. J. Schoelkopf, *Applied Physics Letters* **107**, 162601 (2015).
- [19] C. Buczek, R. Freiberg, and M. Skolnick, *Proceedings of the IEEE* **61**, 1411 (1973).
- [20] L. S. Bishop, J. Chow, J. Koch, A. Houck, M. Devoret, E. Thuneberg, S. Girvin, and R. Schoelkopf, *Nature Physics* **5**, 105 (2009).
- [21] T. Hönigl-Decrinis, R. Shaikhaidarov, S. De Graaf, V. Antonov, and O. Astafiev, *Physical Review Applied* **13**, 024066 (2020).
- [22] Y. Mu and C. M. Savage, *Physical Review A* **46**, 5944 (1992).
- [23] P. R. Rice and H. J. Carmichael, *Physical Review A* **50**, 4318 (1994).

**Supplementary material for "Overcoming photon blockade in circuit QED
single-atom maser with engineered metastability and strong coupling"**

arXiv:2209.05165v1 [quant-ph] 12 Sep 2022

I. GENERAL MEASUREMENT NOTES

Our experiments were done in two cooldowns of the dilution refrigerator. Single-tone and two-tone spectroscopy for device characterization (including S. 3, 4 and Fig. 4(a) of the main text) and auxiliary resonator characterization were done in the first cooldown, and all the other measurements – during the second cooldown. In the second cooldown the attenuation in the input line was increased by 15 dB.



S. 1. **(a-c)** Fit of the reservoir resonator (VNA power at -50 dBm) **(d-g)** Frequency, internal Q-factor (Q_i), external Q-factor (Q_e) and loaded Q-factor (Q_l), respectively, depending on power.

II. DEVICE PARAMETERS

A. Reservoir resonator

The parameters of the reservoir resonator were measured using VNA when the qubit was far detuned from the resonator. Complex VNA traces were fitted using Python package *resonator_tools* [1] and shown in S. 1(a-c); extracted values for the resonance frequency and the quality factors are shown in S. 1(d-g).

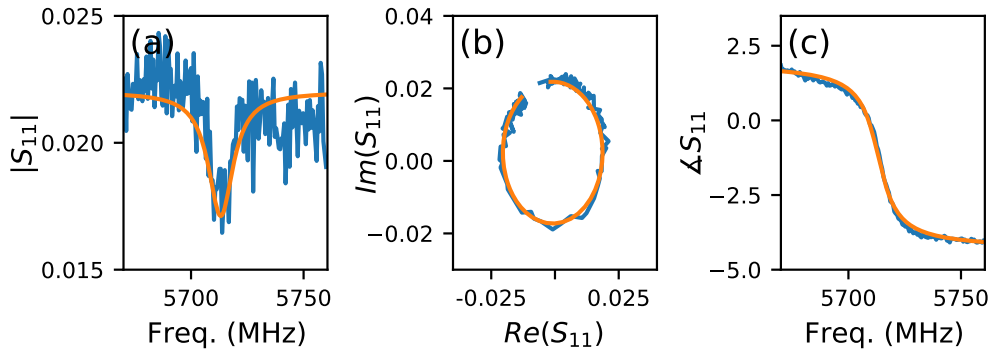
Afterwards, reservoir frequency was assumed to be $f_r = 5.860$ GHz in numerical simulations and all other calculations. The dissipation parameters were calculated from the fitted Q-factors: $\kappa_r = 0.69 \mu\text{s}^{-1}$, $\kappa_r^e = 0.3 \mu\text{s}^{-1}$. The quality factors changed slightly between the cooldowns, but qualitatively it did not affect lasing properties (see S. 6).

B. Auxiliary resonator

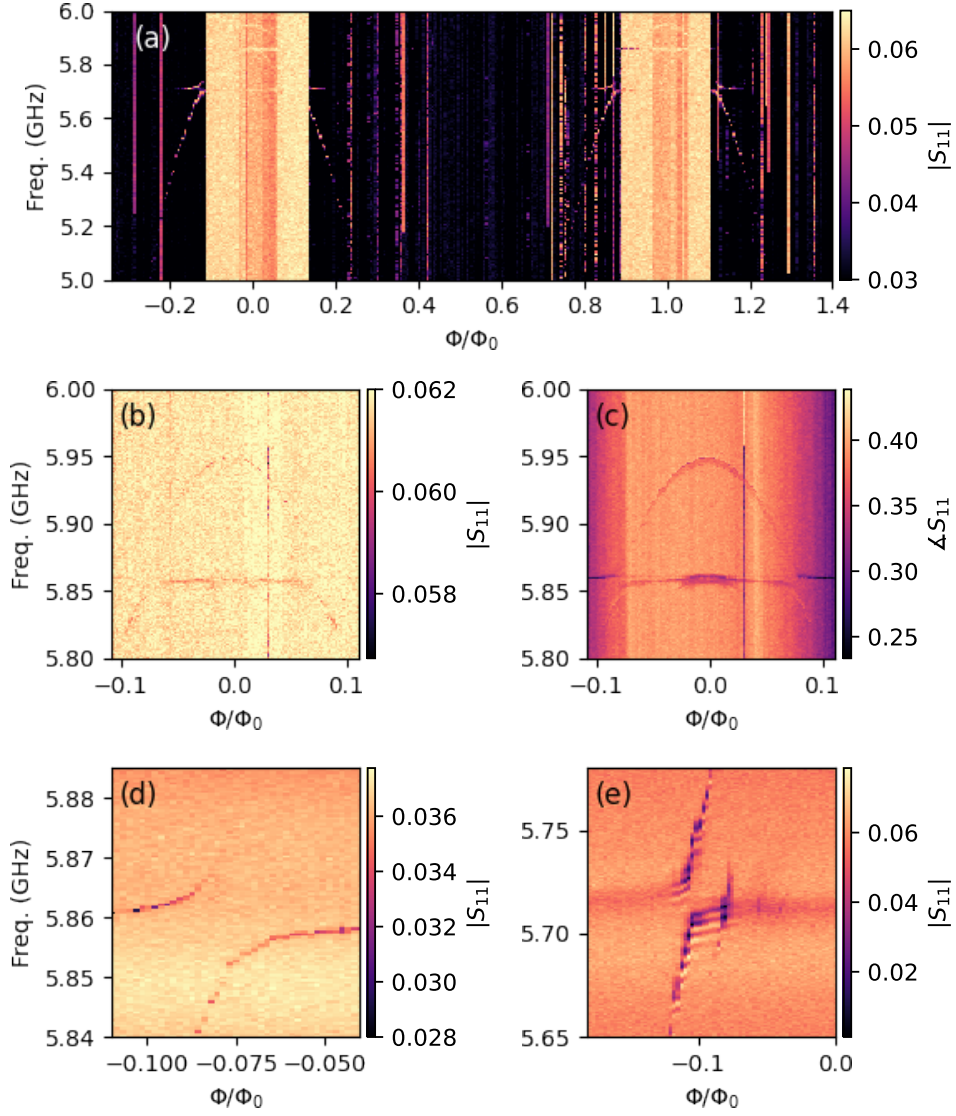
Automatic fitting of auxiliary resonator was not feasible difficult due to its low Q-factor; the data was fitted manually (see S. 2) and the loaded Q-factor was estimated to be around 400. The following values were used for simulations: $f_a = 5.715$ GHz, $\kappa_a = 90 \mu\text{s}^{-1}$.

C. Transmon and coupling

The transmon parameters were found using two-tone spectroscopy (S. 3(a-c)) with an additional microwave source. Its maximal frequency is $f_{ge}^{\text{max}} = 5.95$ GHz, as one can see from S. 3(b,c).



S. 2. (a-c) Manual fit of the auxiliary resonator (VNA power at -50 dBm)



S. 3. **(a)** Two-tone spectroscopy of two periods of the transmon. Two resonator lines at 5.86 GHz and 5.715 GHz are also visible. **(b,c)** Amplitude and phase of two-tone spectroscopy near the $f_{ge}^{\max} = 5.95$ GHz. Reservoir line at 5.86 GHz is visible. **(d)** Single-tone spectroscopy of the avoided crossing with the reservoir. **(e)** Single-tone spectroscopy of the avoided crossing with the auxiliary resonator.

In S. 3(c) when $\Phi_e/\Phi_0 = 0$, there is an additional pair of anticrossings with reservoir resonator, which is caused by coupling of two-photon $|g\rangle \leftrightarrow |f\rangle$ transition with reservoir. Based on these data, the frequency of that transition is equal to f_r and find transmon anharmonicity $\alpha = -180$ MHz.

To find the coupling of the qubit to the cavities, we use single-tone spectroscopy (S. 3(d,e)).

From S. 3(d) we estimate that coupling with reservoir resonator is $g_r/2\pi = \Delta/2 = 11$ MHz, where Δ is the splitting of the anticrossing. Similarly, the coupling with the auxiliary cavity from S. 3(e): $g_a/2\pi = 15.5$ MHz. Periodic spectral features of unknown nature are noticeable in that avoided crossing.

III. PHOTON NUMBER CALIBRATION

Steady-state population N_{ss} in reservoir resonator can be calculated from emitted power, measured by spectrum analyzer, by the following equation:

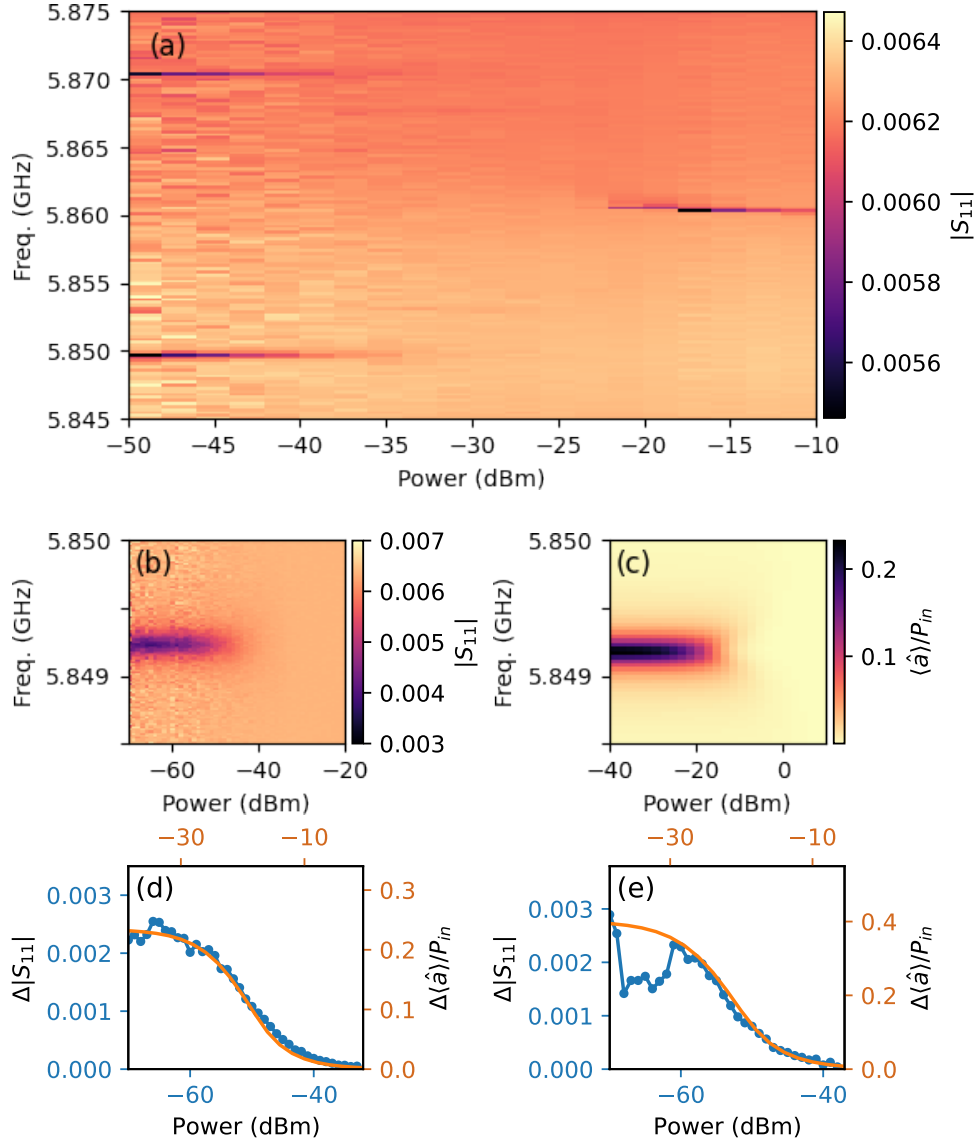
$$N_{\text{ss}} = \frac{P_e}{\kappa_r^e h f_r}, \quad (1)$$

where P_e is integral emitted power in Watts and

$$P_e = P_{\text{SA}}/G, \quad (2)$$

where G is amplification in output line and P_{SA} is the emission power measured by the signal analyzer. G is the only unknown parameter and the task to calibrate N_{ss} is reduced to amplification calibration.

To do that, we first need to measure the saturation of the transmon-reservoir anticrossing under the influence of increasing VNA power P_{VNA} and compare it with the simulation. In S. 4(a), one can observe a smooth transition from a pair of spectral lines to a single line. Then, the top and bottom lines are measured separately with higher resolution (the bottom line is in S. 4(b), the top line is not shown). The next step is a numerical simulation of S. 4(b), which is shown in S. 4(c); we plot the magnitude of the mean value of the annihilation operator $|\langle \hat{a}_r \rangle|$ of the reservoir, which is proportional to $|S_{11}|$. Next, we fit vertical slices of S. 4(b) and (c) with Lorentzian curves and plot the amplitude of the dip (peak) depending on power both for experiment and simulation. We also repeat this procedure for top line of the avoided crossing. The final results for two lines are in S. 4(d) and (e). By comparing the values on the x -axes of the experimental and simulated plots, we find a difference of 31.5 dBm (this value is the same for both lines). The driving amplitude in our simulation depends not only on the absolute power at the cavity coupling port $P_{\text{c.p.}}$, but also on the external quality factor of the cavity, so this difference is not enough for calibration. We make another simulation with turned-off coupling between the cavity and the transmon, and then



S. 4. **(a)** Single-tone spectroscopy of qubit-reservoir anticrossing depending on VNA power. Lasing pumping is turned off. **(b)** Single-tone spectroscopy of bottom line of the anticrossing on (a) depending on VNA power. **(c)** Simulation of single-tone spectroscopy on (b): $\langle \hat{a} \rangle$ of reservoir depending on direct resonator pumping frequency and power. **(d)** Amplitude of Lorentz dip of $|S_{11}|$ from (b) (blue) and of Lorentz peak of $\langle \hat{a} \rangle$ from (c) (orange) depending on VNA power. **(e)** Same as (d), but for top line (analogous to (b) and (c) pictures are not shown)

compare the result to a common formula for a bare cavity photon population,

$$N_{\text{ph}} = \frac{4\kappa_r^e}{\hbar f_r \kappa_r^2} P_{\text{c.p.}} \quad (3)$$

In this additional simulation, for -3.5 dBm we obtain $N_{\text{ph}} = 33.5$. Then we know that the same population is reached in experiment for $P_{\text{VNA}} = -3.5 - 31.5 = -35$ dBm. Using (3), we find that line attenuation $A = P_{\text{VNA}}/P_{\text{c.p.}} = 102.8$. We check that this value adds up well from the approximately 70 dB in the attenuators inside the refrigerator, 20 dB in the directional coupler that was used for two-tone spectroscopy and 10 dB of loss in the cables.

Consequently, if the input power is -40 dBm, then $P_{\text{c.p.}} = -142.8$ dBm. Knowing this fact, we can find the amplification G of output line. To do it, we set input power to -40 dBm, frequency to 5.9 GHz (to be not very far from working frequency) and measure the reflected power by spectrum analyzer, assuming that reflected power outside the resonance is almost equal to $P_{\text{c.p.}}$. The measured power is 78.8 dBm, which means that $G = 78.8 - (-142.8) = 64$ dBm. Now we can use Eq. 1 to calculate N_{ss} for any output power.

IV. SIMPLIFIED ANALYTICAL MODEL WITH DETUNING

Since in the experimental configuration the ef transition of the qubit is detuned by 35 MHz from the $|0\rangle_a \rightarrow |1\rangle_a$ transition, the calculation in Sec. IV of the theoretical proposal [2] has to be modified. Precisely, we again need to solve the GKSL master equation, but now with a non-zero detuning included into the Hamiltonian:

$$\hat{H}_{\text{t-a}}/\hbar = g_a(ba_a^\dagger + b^\dagger a_a) + \delta b^\dagger b, \quad (4)$$

where a_a is truncated to two lowest levels and b to two levels e and f (meaning that the effective coupling constant should be changed to $g = g_a\sqrt{2}$). For this calculation, the dissipative part in the master equation contains only the collapse operator $\sqrt{\kappa_a}a_a$. We find that solving the resulting ODE system is easier in the real-number representation of the density matrix. If the corresponding transformation is done as $\rho_r = \mathcal{T}\rho$ with some superoperator \mathcal{T} , then the GKSL equation is transformed to

$$\dot{\rho}_r = \mathcal{L}_r \rho_r, \quad (5)$$

where $\mathcal{L}_r = \mathcal{T}\mathcal{L}\mathcal{T}^{-1}$ is also real. Finding the effective decay rate γ_{ef}^{eff} of the ef -transition (κ_a^{eff} in the notation of [2]) is now equivalent to finding the slowest-decaying non-oscillating exponent in

the solution. The relevant eigenvalue of \mathcal{L} turns out to be

$$\begin{aligned}\lambda &= -\gamma_{ef}^{\text{eff}} = -\frac{\kappa_a}{2} + \sqrt{\gamma^2 + 2g_\delta^2}, \\ \gamma^2 &= \frac{\kappa_a^2}{8} - \frac{\delta^2}{2} - 2g^2, \\ g_\delta^2 &= \sqrt{\left[\frac{\delta^2}{4} + \left(g + \frac{\kappa_a}{4}\right)^2\right] \left[\frac{\delta^2}{4} + \left(g - \frac{\kappa_a}{4}\right)^2\right]}.\end{aligned}\tag{6}$$

For the experimental parameters $g/2\pi = 21.9$ MHz, $\kappa = 90 \mu\text{s}^{-1}$, $\delta/2\pi = 35$ MHz, we find $\gamma^2 \approx -61.1 \cdot 10^3 \mu\text{s}^{-2}$, $g_\delta^2 \approx 30.9 \cdot 10^3 \mu\text{s}^{-2}$ and $\gamma_{ef}^{\text{eff}} \approx 17 \mu\text{s}^{-1}$. One can compare this value with the resonant under-damped case where $\gamma_{ef}^{\text{eff}} = \kappa_a/2 = 45 \mu\text{s}^{-1}$ [2].

Another way to calculate γ_{ef}^{eff} is to find the steady state solution of the master equation with an addition of a weak incoherent excitation $|e\rangle \rightarrow |f\rangle$ at rate $\tilde{\Gamma}$. Lifting the two-level approximation for the cavity, we rewrite (4) as the Jaynes-Cummings model with detuning

$$\hat{H}_{t-a}/\hbar = g(\sigma_{ef}^- a_a^\dagger + \sigma_{ef}^+ a_a) + \delta \sigma_{ef}^+ \sigma_{ef}^-, \tag{7}$$

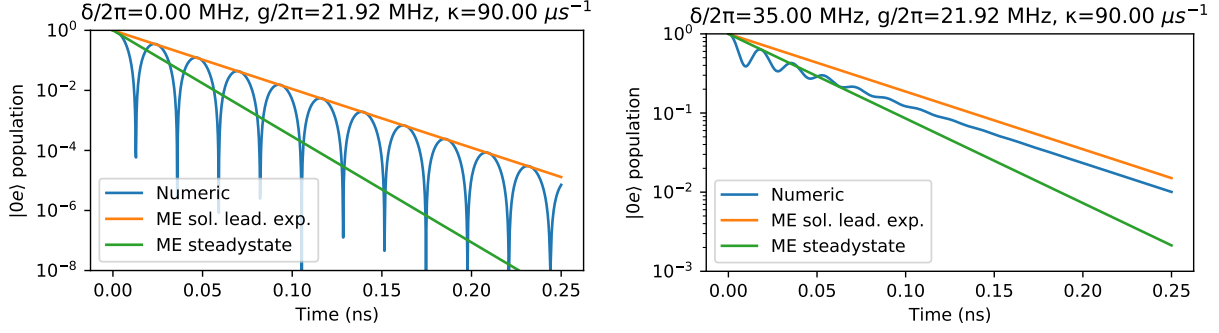
where $g = \sqrt{2}g_a$, and insert the collapse operators $\sqrt{\kappa_a}a_a$ and $\sqrt{\tilde{\Gamma}}\sigma_{ef}^+$ in the GKSL equation. In matrix form for the vector of the steadystate expectation values $\mathbf{x}_{\text{ss}} = [\langle a_a^\dagger a_a \rangle_{\text{ss}}, \langle \sigma_{ef}^+ \sigma_{ef}^- \rangle_{\text{ss}}, \langle \sigma_{ef}^+ a_a + \sigma_{ef}^- a_a^\dagger \rangle_{\text{ss}}, \langle \sigma_{ef}^+ a_a - \sigma_{ef}^- a_a^\dagger \rangle_{\text{ss}}]^T$ it reads:

$$\begin{bmatrix} -\kappa_a & 0 & 0 & ig \\ 0 & -\tilde{\Gamma} & 0 & -ig \\ 0 & 0 & -\kappa_a/2 - \tilde{\Gamma}/2 & i\delta \\ 2ig - 4ig\alpha & -2ig & i\delta & -\kappa_a/2 - \tilde{\Gamma}/2 \end{bmatrix} \mathbf{x}_{\text{ss}} = \begin{bmatrix} 0 \\ -\tilde{\Gamma} \\ 0 \\ 0 \end{bmatrix}.\tag{8}$$

Here, to linearize the system we replace the term $-4ig \langle \sigma_{ef}^+ \sigma_{ef}^- a_a^\dagger a_a \rangle_{\text{ss}}$ in the last equation by $-4ig \langle a_a^\dagger a_a \rangle_{\text{ss}} \alpha$, where $\alpha = \langle \sigma_{ef}^+ \sigma_{ef}^- \rangle_{\text{ss}}$, neglecting the correlation between the qubit and resonator populations. In the steady state, the balance condition $\gamma_{ef}^{\text{eff}} \langle \sigma_{ef}^+ \sigma_{ef}^- \rangle_{\text{ss}} = \kappa_a \langle a_a^\dagger a_a \rangle_{\text{ss}}$ is satisfied, meaning that the rate of qubit population leakage must be equal to the rate of the cavity population leakage, since there is no other dissipation channel for the former. In the limit of $\tilde{\Gamma} \rightarrow 0$ and $\alpha \rightarrow 0$ we obtain

$$\gamma_{ef}^{\text{eff}} = \frac{\kappa_a \langle a_a^\dagger a_a \rangle_{\text{ss}}}{\langle \sigma_{ef}^+ \sigma_{ef}^- \rangle_{\text{ss}}} \approx \frac{4g^2 \kappa_a}{4\delta^2 + 4g^2 + \kappa_a^2}.\tag{9}$$

This expression has a more compact form than (6). We check that $\alpha \ll 1$ if $\tilde{\Gamma} \lesssim 5 \mu\text{s}^{-1}$ by solving the quadratic self-consistency equation $\alpha = \langle \sigma_{ef}^+ \sigma_{ef}^- \rangle_{\text{ss}}$ for α . For the experimental parameters,



S. 5. Comparison between the numerical solution (blue curve) and the two analytic solutions (6), (9) (orange and green curves, respectively).

from (9) $\gamma_{ef}^{\text{eff}} \approx 25 \mu\text{s}^{-1}$. The comparison between the numerical solution, (6), and (9) is shown in S. 5 in log-scale; one can see that (9) predicts higher decay rate compared to the time-dependent solution though being closer to the numerical result in terms of RMS distance.

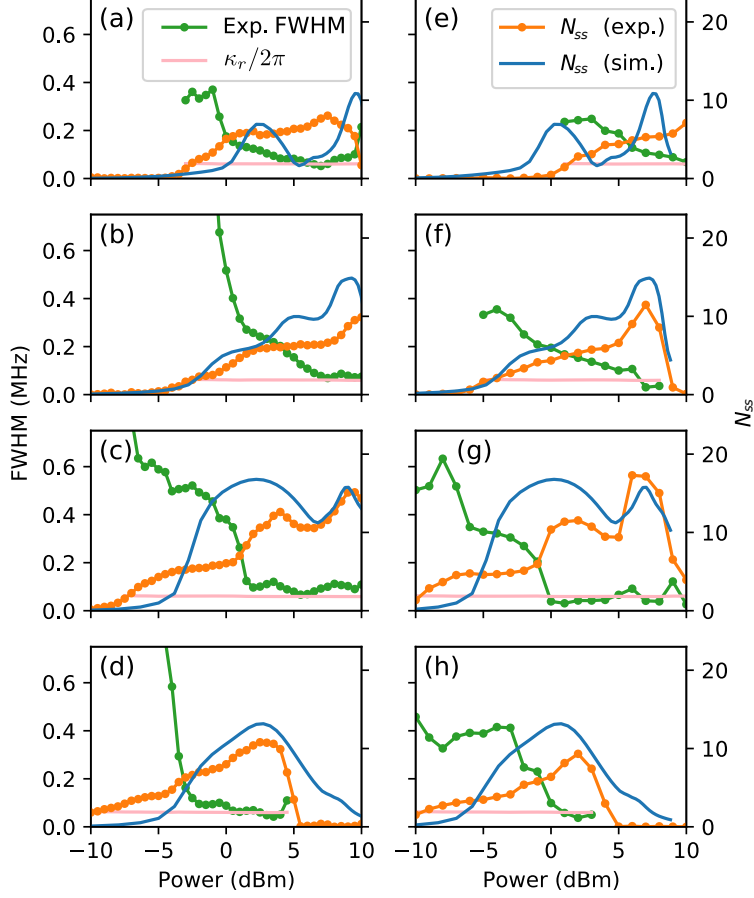
Next, we estimate the effective pumping rate from $|g\rangle \rightarrow |e\rangle$ when the two-photon ef transition Rabi frequency is $\Omega_{2\text{ph}}$. Compared to the proposal, the experimental value of γ_{ef}^{eff} is now closer to the estimated $\Omega_{2\text{ph}}$ so that the strong-coupling case $\gamma_{ef}^{\text{eff}} < 2\Omega_{2\text{ph}}$ may be reached. That means that the pumping rate $\Gamma = \gamma_{ef}^{\text{eff}}/2 \approx 8.5 \mu\text{s}^{-1}$ by (6) or even $12.5 \mu\text{s}^{-1}$ by (9), compared to $5.3 \mu\text{s}^{-1}$ calculated before for the optimal parameters in the resonant case [2]. One can see that non-zero detuning does not deteriorate the effective pumping rate if compensated by the strong coupling regime of the two-photon pump.

Finally, we estimate the resulting expected population of the reservoir N_{ss} . The strong coupling condition $4\sqrt{N}g_r > N\kappa_r$ is met for $\kappa_r = 0.69 \mu\text{s}^{-1}$, $g_r/2\pi = 11 \text{ MHz}$ for $N < 360$, so the expected population for the more modest Γ value predicted by (6) is

$$N_{\text{ss}} = 2\frac{\Gamma}{\kappa_r} \approx 24. \quad (10)$$

V. NUMERICAL SIMULATION

Besides the analytical calculation, we use a full numerical model to check our results in a similar manner to the theoretical proposal [2]. The simulation was performed using Python package QuTiP [3]. The parameters used in simulation were taken from the experiment (see Table 1 of the main text): $f_r = 5.860 \text{ GHz}$, $\kappa_r = 0.69 \mu\text{s}^{-1}$, $f_a = 5.715 \text{ GHz}$, $\kappa_a = 90 \mu\text{s}^{-1}$, $g_r/2\pi = 11 \text{ MHz}$, $g_a/2\pi = 15.5 \text{ MHz}$. We assume that the transmon frequency is set to $f_{ge} = 5.863 \text{ GHz}$, and



S. 6. **(a-d)** First cooldown: number of pumped photons (experiment and simulation) and FWHM (experiment and pure reservoir resonator) for different pumping frequencies ω_{drive} : (a,e) 5.7775 GHz, (b,f) 5.7825 GHz, (c,g) 5.7875 GHz – exact two-photon frequency, (d,h) 5.7925 GHz. **(e-h)** Second cooldown, parameters same as in the first cooldown.

the two-photon pumping frequency to be $f_p/2\pi = \frac{f_r+f_a}{2} = 5.7875$ GHz, which was used in the experiment, unless otherwise stated.

The results of N_{ss} depending on the pump power for different f_p are shown on S. 6 in comparison with the experiment for the two cooldowns. One can see that the experimental behavior reproduces itself with good accuracy from cooldown to cooldown. We note that numerical N_{ss} agrees much better with the experimental results than the simple model prediction from the previous section, even replicating the self-quenching effects at high pumping powers.

VI. SAMPLE FABRICATION

A transmon qubit in this study is composed of two Al/AIO_x/Al Josephson junctions (asymmetric SQUID) and a shunting capacitor. The JJs are patterned by electron lithography. The aluminum film is evaporated in HV e-beam system and the JJs are formed by double-angle Dolan bridge technique [4, 5] followed by lift-off. To build a ground plane, 100 nm aluminum film is evaporated on a silicon substrate and etched in Cl₂ plasma after optical lithography. To improve the interface between the substrate and the ground metal we remove the native oxide by dipping the silicon wafer in piranha solution and buffered HF [6, 7] before aluminum evaporation. To obtain a good galvanic contact between the transmon qubit and the ground plane, it is further shorted by additional aluminum bandage layer [8]. We also implement aluminum air-bridges on the top of the coplanar transmission lines [9].

-
- [1] S. Probst, F. B. Song, P. A. Bushev, A. V. Ustinov, and M. Weides, *Review of Scientific Instruments* **86**, 024706 (2015).
 - [2] A. Sokolova, G. Fedorov, E. Il'ichev, and O. Astafiev, *Physical Review A* **103**, 013718 (2021).
 - [3] J. R. Johansson, P. Nation, and F. Nori, *Computer Physics Communications* **183**, 1760 (2012).
 - [4] G. J. Dolan, *Appl. Phys. Lett.* **31**, 337 (1977).
 - [5] L. Liechao, J. Kang, and J. Wen, *ECS Transactions* **44**, 481 (2012).
 - [6] A. Bruno, G. de Lange, S. Asaad, K. L. van der Enden, N. K. Langford, and L. DiCarlo, *Applied Physics Letters* **106**, 182601 (2015), <https://doi.org/10.1063/1.4919761>.
 - [7] D. Kalacheva, G. Fedorov, A. Kulakova, J. Zotova, E. Korostylev, I. Khrapach, A. V. Ustinov, and O. V. Astafiev, *AIP Conference Proceedings* **2241**, 020018 (2020), <https://aip.scitation.org/doi/pdf/10.1063/5.0011900>.
 - [8] A. Osman, J. Simon, A. Bengtsson, S. Kosen, P. Krantz, D. P. Lozano, M. Scigliuzzo, P. Delsing, J. Bylander, and A. Fadavi Roudsari, *Applied Physics Letters* **118**, 064002 (2021), <https://doi.org/10.1063/5.0037093>.
 - [9] Z. Chen, A. Megrant, J. Kelly, R. Barends, J. Bochmann, Y. Chen, B. Chiaro, A. Dunsworth, E. Jeffrey, J. Y. Mutus, P. J. J. O'Malley, C. Neill, P. Roushan, D. Sank, A. Vainsencher, J. Wenner, T. C. White, A. N. Cleland, and J. M. Martinis, *Applied Physics Letters* **104**, 052602 (2014).